Journal of
Materials Chemistry A

Accepted Manuscript

This article can be cited before page numbers have been issued, to do this please use: F. Pan, A. Liang, Y. Duan, Q. Liu, J. Zhang and Y. Li, *J. Mater. Chem. A*, 2017, DOI: 10.1039/C7TA03005C.

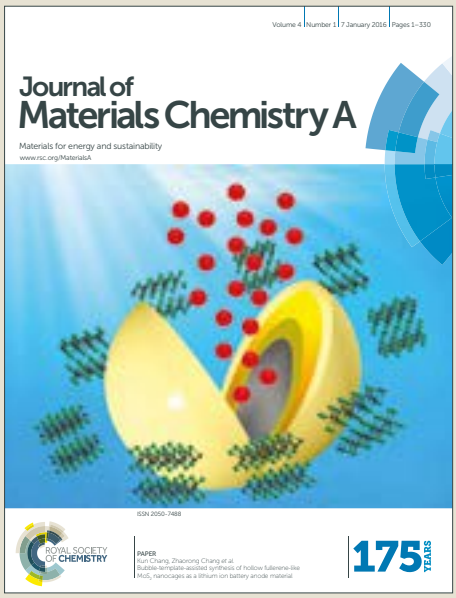

ROYAL SOCIETY OF CHEMISTRY

rsc.li/materials-a

View Article Online
DOI: 10.1039/C7TA03005C

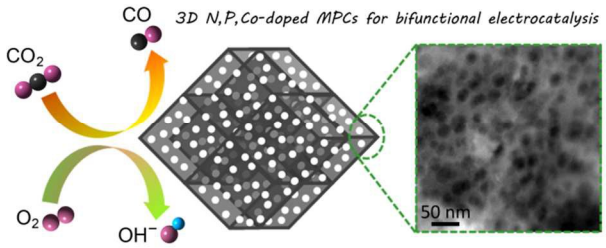

3D N,P,Co-doped mesoporous carbon frameworks synthesized via a new self-growth-templating approach enable efficient bifunctional electrocatalysis in ORR and CO2RR

ROYAL SOCIETY OF CHEMISTRY View Article Online
DOI: 10.1039/C7TA03005C

Journal of Materials Chemistry A

ARTICLE

Self-Growth-Templating Synthesis of 3D N,P,Co-Doped Mesoporous Carbon Frameworks for Efficient Bifunctional Oxygen and Carbon Dioxide Electroreduction

Received 00th January 20xx,
Accepted 00th January 20xx

DOI: 10.1039/x0xx00000x

www.rsc.org/

Fuping Pan,[a,b] Aimin Liang,[a] Youxin Duan,[a] Qiao Liu,[c] Junyan Zhang,*[a] and Ying Li*[b]

Although mesopore designs are expected to play a key role in exploring electrocatalytic properties of carbons, facile preparation of mesoporous carbons (MPCs) with efficient dopants to enable high performance remains a great challenge. Herein, we for the first time introduce a self-growth-templating concept for the fabrication of three-dimensional (3D) N,P,Co-doped MPCs frameworks, simply through pyrolysis of Vitamin B_{12} in NaCl assemblies-enclosed nanoreactors. The route realizes the controllable formation of mesoporous templates, elimination of the templates, as well as in situ doping of N,P,Co into MPCs in a one-step enclosed-space-assisted pyrolysis process. The highly mesoporous architecture not only enhances mass transportation but also provides the 3D electrocatalyic surface to expose highly active N,P,Co-induced dopants. These features endow MPCs with excellent activity as bifunctional electrocatalysts in oxygen reduction ($E_{1/2}$ of 0.85 V, J_K of 51 mA cm^{-2} at −0.71 V and Tafel slope of 53 mV dec^{-1}) and CO_2 reduction reactions (overpotential of −0.19 V, maximum FE of 62% for CO and Tafel slope of 129 mV dec^{-1}), coupled with high electrochemical stability in aqueous electrolytes. We expect that the self-constructing vision can afford useful insights to guide the development of other advanced mesoporous materials beyond carbon for broad applications.

Introduction

Mesoporous carbons (MPCs) are receiving growing interest in a wide range of applications. In particular, recent progresses have demonstrated that MPCs functionalized with heteroatoms may hold great promise as electrocatalysts in various energy-related electrochemical reactions.[1-3] Among them, oxygen reduction reaction (ORR) and carbon dioxide reduction reaction (CO2RR) are of great significance. The ORR is known to be at the heart of fuel cells and metal-air batteries, and the CO2RR offers a sustainable approach to convert greenhouse CO_2 into value-added fuels by using renewable energy as input electric energy. However, the sluggish nature of kinetics rates for ORR/CO2RR and lack of the advanced electrocatalysts with earth-abundant elements and high performance impede their practical applications.[4-6] By virtue of intriguing features of mesoporous network including numerous edge locations, large interfacial area, and porous channel that can enhance the number of dopants, accessibility of active centers, and mass transportation in an electrochemical process,[1,7-10] employing MPCs as the electrocatalysts to expedite the kinetics rates for the ORR and CO2RR may represent a promising solution to boost large-scale implementations of these clean-energy technologies.

So far, considerable effort has been made to the design of MPCs in electrocatalysis, and templating methods (hard and soft templates) are of utmost common and significance thanks to their potential scalability and ability to tune pore sizes.[11,12] The assembly of carbon/heteroatoms precursors with external templates (e.g., silica, block copolymers) followed by high-temperature carbonization is necessary to construct MPCs and introduce heteroatoms. For example, N/S/Fe-doped MPCs have been developed by the external-templating methods and applied in catalyzing the ORR.[11-16] However, external-templating strategies are not ideal for the fabrication of MPCs to achieve high electrocatalytic performance. The major drawbacks are that the insufficient assembly due to weak interactions between the templates and precursors, aggregation of the nano-sized templates, and post-doping processes may lead to a poor mesoporous structure and low-density distribution of dopants, causing negative effects on electrocatalytic properties of MPCs. Furthermore, the external-templating methods commonly require rather elaborated procedures and/or toxic reagents to synthesize and eliminate the templates, rendering disadvantages to the scale-up production. Thereby, the excellence of MPCs in electrocatalysis would not be fully realized before the facile approach to synthesize MPCs that could also achieve the in

[a] State Key Laboratory of Solid Lubrication, Lanzhou Institute of Chemical Physics, Chinese Academy of Science, Lanzhou 730000, China
Email: zhangjunyan@licp.cas.cn
[b] Department of Mechanical Engineering, Texas A&M University, College Station, TX 77843, USA
Email: yingli@tamu.edu
[c] Institute of Materials, Ningbo University of Technology, Ningbo 315016, China
Electronic Supplementary Information (ESI) available: additional materials characterization and electrochemical data. See DOI: 10.1039/x0xx00000x

situ incorporation of the highly active and dense dopants is available from pore-accelerating electrocatalysis perspective.

We hypothesize that, rather than employing the extrinsic templates, if the thermally unstable mesoporous templates would be evolved from the heteroatoms precursors themselves in a temperature-programmed procedure, the thermal decomposition of the self-growth templates at a high temperature can thus not only yield the mesopore facilely but also provide additional sources to accomplish the effective insertion of the heteroatoms. This is the primary motivation of the present work. Inspired by this vision, herein, we report for the first time a new self-growth-templating concept to realizing the facile synthesis of three-dimensional (3D) N,P,Co-doped MPCs frameworks. Specifically, the mesopore is constructed via a mechanism involving the self-formation of the thermally unstable mesoporous templates from the carbonization of Vitamin B_{12} enclosed in a space-sealed nanoreactor provided by NaCl self-assemblies. The subsequent thermolysis of the self-constructed templates at the high temperature liberates the mesopore and more importantly, the in situ doping of N, P and Co into the MPCs matrix is also achieved during the overall pyrolysis process since the templates are also useful feedstock for the generation of dopants. The resultant MPCs are characterized by 3D carbon honeycombs, large-sized mesopore (about 30 nm), high surface area (1036 m^2 g^{-1}), and dense distribution of the N,P,Co dopants. Accordingly, MPCs can serve as high-performance bifunctional electrocatalysts for the ORR and CO2RR, which are attributed to the efficient utilization of N,P,Co-induced active functionalities and the promotion of mass transfer afforded by 3D highly mesoporous architecture.

Results and discussion

Our approach for synthesizing MPCs is schematically depicted in Fig. 1. In the first step, the Vitamin B_{12} and NaCl were dissolved in water and stirred to generate well-dispersed solution. In the second step, the mixture was freeze-dried to remove water, which also ensures the preservation of a homogeneous dispersion of the Vitamin B_{12} and NaCl. Moreover, NaCl particles were spontaneously self-assembled into 3D NaCl aggregates thanks to the cubic structural characteristic of the NaCl during this stage,[17] and Vitamin B_{12} layers were coated onto the surface of the NaCl, labeled as VB-NaCl. SEM images (Fig. S1) clearly indicates that VB-NaCl is made of the closely packed NaCl assemblies with the sizes of about 1000 nm. The subsequent annealing of VB-NaCl in Ar ambiance at 900 ^{o}C combined with the elimination of the NaCl by water yielded MPCs frameworks (named as MPC-900) (third step).

The morphology and porous structure of MPC-900 were systematically investigated by electron microscopic techniques. SEM, TEM and STEM images show that MPC-900 is comprised of the highly interconnected 3D carbon with macroporous frameworks and a substantial amount of through and in-plane mesopores (Fig. 2A, B, E). The magnified images further clearly confirm the well-defined mesopores with the sizes mostly

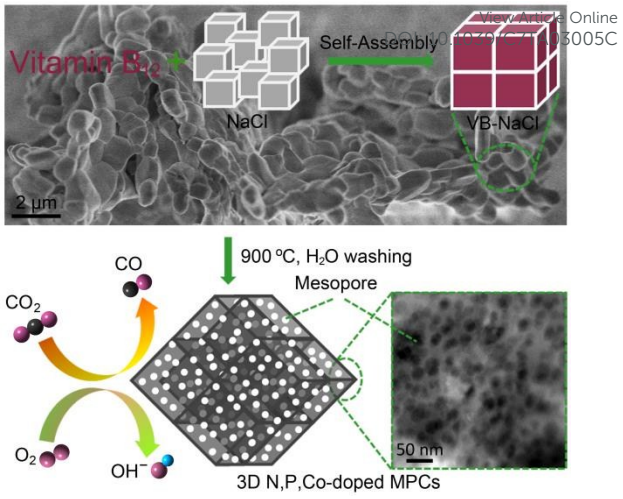

Fig. 1 A schematic illustration of the fabrication procedure for MPCs.

within around 30 nm, which are randomly but densely distributed in 3D carbon walls (Fig. 2C, D, F). The elemental mapping images disclose the uniform dispersion of P, N and Co elements on the porous carbon skeleton (Fig. 2G). These characterizations demonstrate that the facile preparation of N,P,Co-doped MPCs frameworks is successfully realized using the Vitamin B_{12} as a single precursor and NaCl as auxiliary via the simple solid-phase pyrolysis route, which does not use the external mesoporous templates.

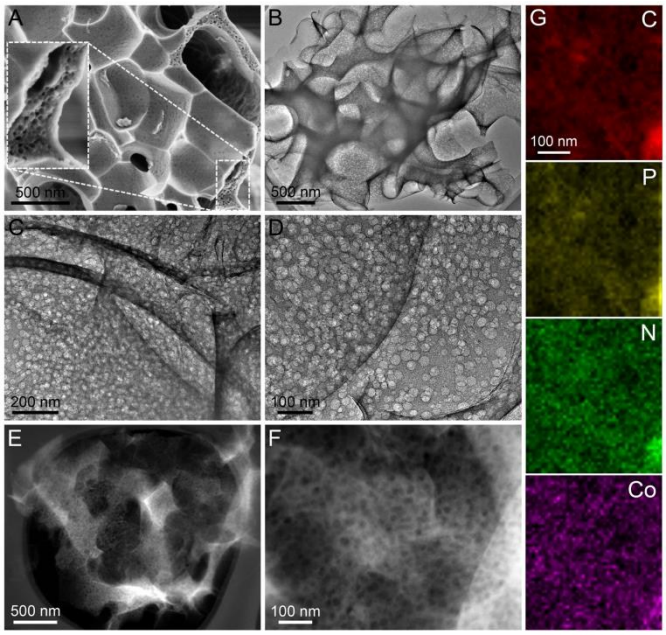

Fig. 2 Typical (A) SEM, (B-D) TEM, and (E-F) STEM images of MPC-900. (G) The C, P, N and Co elements mapping images of the selected area in Fig. S2B for MPC-900.

To better understand the mesopore formation process and mechanism, multiple control experiments were conducted. To unveil the role of the NaCl, the synthesis was performed in the same manner as for MPC-900, except the omission of NaCl addition, and the resultant sample was designated as VB-X (X refers to annealing temperature). For VB-900, only thick carbon plates with a remarkable quantity of Co_2P nanoparticles encapsulated by carbon shells are observed (Fig. S3), which significantly differs from characteristics of MPC-900 prepared with the NaCl. This result manifests that the assembled NaCl aggregates are indispensable for the generation of the mesopore, and the 3D honeycomb-like morphology of MPC-900 might be derived from the duplication of the NaCl assemblies.

The mesopore formation was further monitored over the heating temperature from 400 to 1000 ^{o}C with an interval of 100 ^{o}C according to the thermogravimetric analysis of Vitamin B_{12} (Fig. S4). For clarity, samples synthesized from the Vitamin B_{12} and NaCl without the mesopore and with the mesopore are denoted as VB-Na-X and MPC-X (X represents the heating temperature), respectively, (Table S1). The TEM results demonstrate that there is absence of the mesopore when the pyrolysis is conducted below 600 ^{o}C, whereas plenty of particles with the sizes similar to the mesopore (~30 nm) are generated, which are well-shaped at 500 ^{o}C and randomly distributed in the 3D carbon walls (Fig. 3A, B, Fig. S5-S8). The X-ray diffraction (XRD) pattern indicates that VB-Na-500 shows an amorphous nature of carbon (Fig. S6B), and the elemental-linear images suggest that the particles may be constituted by O,P,Co motifs (Fig. S7), albeit the fine composition and structure of these particles are still not well known. By contrast, VB-500 prepared using the Vitamin B_{12} alone at 500 ^{o}C is free of the particles (Fig. 3C), manifesting the vital role of the NaCl for the production of the O,P,Co-containing particles. Surprisingly, the intermediate particles are disappeared and the mesopores are formed at 700 ^{o}C (Fig. S9). We noticed that, especially at a higher temperature above 800 ^{o}C, the well-defined mesopore will be generated (Fig. S10-S11), revealing the crucial function of the pyrolysis temperature in controlling the evolution of the mesopore. N_2 adsorption-desorption tests (Fig. S12) were performed to determine the pore size distributions. As presented in Fig. 3D, the obvious mesopores centered at about 30 nm are observed in MPC-X, while no large-sized mesopore is generated in VB-900 and VB-Na-X, consistent well with TEM observations. The specific surface area of MPC-900 is calculated to be 779 $m^2 g^{-1}$ (1036 $m^2 g^{-1}$ for MPC-1000), which are over 30 times higher than 24 $m^2 g^{-1}$ for VB-900 thanks to the mesopore in MPC-900. The difference in the structure of intermediates unambiguously verifies that the NaCl assemblies and heating temperature together play the decisive role in the growth of the intermediate particles and final mesopores.

On the basis of implications of results presented above, a self-growth-templating mechanism is proposed to explain the mesopore formation (Fig. 3E). The tightly packed VB-NaCl aggregates are formed first from the self-assembly of Vitamin B_{12} and NaCl mixture in the lyophilization process. In the

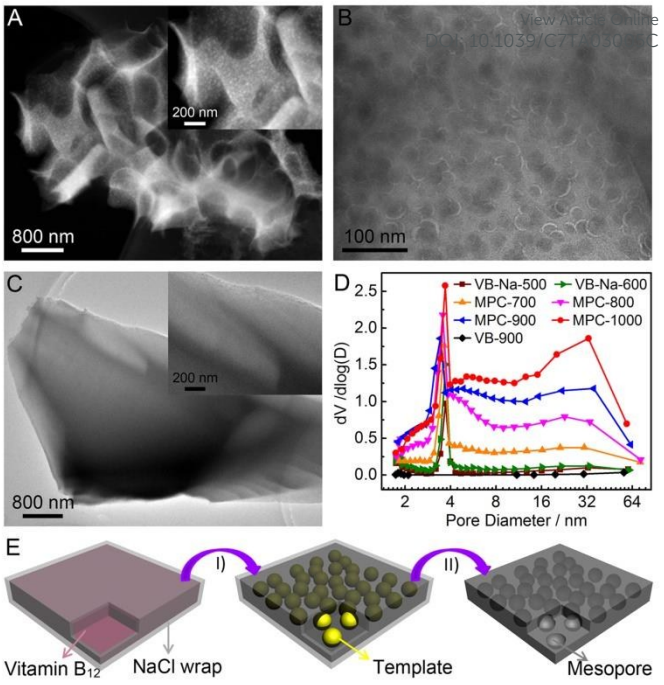

Fig. 3 (A) STEM and (B) TEM images of VB-Na-500. (C) TEM images of VB-500. (D) The pore size distributions of VB-900, VB-Na-X and MPCs. (E) A proposed mechanism for the mesopore evolution: (I) Self-generation of the mesoporous templates from pyrolysis of the Vitamin B_{12} in sealed surroundings by the NaCl assemblies wrapping at 500 ^{o}C; (II) Releasing the mesopore after the thermal decomposition of the templates at above 700 ^{o}C and elimination of NaCl by water.

aggregates, the NaCl particles are covered by Vitamin B_{12} layers, and Vitamin B_{12} coatings are entirely surrounded by the NaCl assemblies; this structure provides sealed surroundings for the Vitamin B_{12}. The carbonization of the Vitamin B_{12} produces the 3D macroporous carbon skeletons on account of the 3D templates function of the NaCl assemblies. More importantly, the thermally unstable particles made of the P,O,Co components are generated spontaneously at the low temperature of 500 ^{o}C, which may be originated from the assistance of the sealed circumstance by the assembled NaCl. The NaCl assemblies may serve as the space-enclosed nanoreactor and prevent P,O,Co groups from uniformly dispersing in carbon, thus leading to the chemical combination of the P,O,Co species and further formation of the intermediate particles with a diameter in about 30 nm embedded in the 3D carbon walls. These unstable particles will be decomposed when the pyrolysis temperature rises to 700 ^{o}C, which thus act as the sacrificial templates to yield the mesopores, along with the in situ insertion of N,P,Co atoms into the porous carbon matrix. The subsequent elimination of NaCl by water releases 3D N,P,Co-doped MPCs frameworks. Note that the melting of NaCl crystal at 805.9 ^{o}C leads to the coverage of MPCs by NaCl molten salt (Fig. S13), which is

beneficial for the graphitization of MPCs,[8] as manifested by Raman results (Fig. S14). This self-constructing recipe does not involve the adoption of additional mesoporous templates, which proceeds through a self-growth-templating pathway. The merit makes the route superior to the conventional external-templating methods in that the self-formed templates can also function as the heteroatoms sources to boost the doping of the functionalities.

X-ray photoelectron spectroscopy (XPS) was performed to detect contents and chemical bonding states of the doped functionalities. The survey spectrum of MPC-900 reveals the presence of the C, N, P, O and Co elements (Fig. S15). The variations of compositions for MPCs are summarized in Table S2. The decrease in the contents of the doped atoms with increasing the heating temperature is probably due to the thermolysis of the unstable groups. The fitted high-resolution P 2p spectra at ~132.9 and ~134.2 eV are indexed to P–C and P–O bonds, respectively (Fig. 4).[18-20] The N 1s spectra can be deconvoluted into four different peaks centered at ~398.7, ~399.8, ~400.9 and ~402.3 eV, which correspond to pyridinic, pyrrolic, graphitic and oxidized nitrogen species, respectively (Fig. 4).[21-24] The pyridinic and pyrrolic N are also believed to bond with the Co and to form Co–N coordinations,[25] as reflected by Co 2p peak centered at about 781.3 eV (Fig. S16a), suggestive of the existence of Co–N_X complex.[26] We observed that, with increasing temperature, conversions from pyridinic/pyrrolic to graphitic N and from P–O to P–C are occurred (Fig. 4), implying that the heating temperature leads to the change of N,P electronic environments in MPCs, in agreement with previous reports on N/P-doped nanocarbons.[27,28] The XRD characterizations indicate that, especially at the high temperature of 1000 °C, the Co_2P nanocrystal is formed (Fig. S16b). These results demonstrate that changes in the compositions and electronic structures of doped N,P,Co depend strongly on the heating temperature, which might have intense influences on the electrocatalytic activities of MPCs.

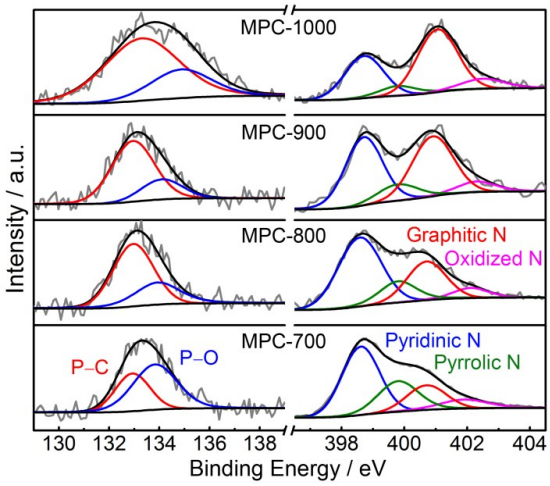

Fig. 4 Deconvoluted P 2p and N 1s spectra for MPCs synthesized at different pyrolysis temperatures.

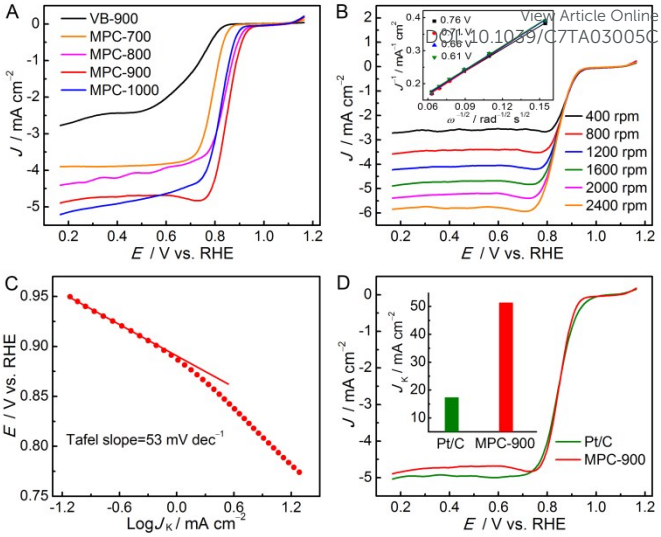

Fig. 5 (A) Linear sweep voltammetry (LSV) curves of VB-900 and MPCs for the ORR in O_2-saturated 0.1 M KOH. Rotating speed: 1600 rpm; scan rate: 5 mV s^{-1}. (B) LSV curves of MPC-900 in O_2-saturated 0.1 M KOH at different rotating speed. Scan rate: 5 mV s^{-1}. Insert is corresponding Kouteckey–Levich (K–L) plots. (C) Tafel plot of MPC-900. (D) LSV curves and kinetic-limiting current density (insert) at −0.71 V of MPC-900 and Pt/C. Rotating speed: 1600 rpm; scan rate: 5 mV s^{-1}.

As pointed out that heteroatoms-doped MPCs are tremendously expected to be effectual in the electrochemical reactions, we thus first evaluated the catalytic capability of as-prepared N,P,Co-doped MPCs frameworks for the ORR, by loading MPCs onto a glassy carbon electrode that serves as working electrode in a three-electrode system in 0.1 M KOH. The cyclic voltammetry (CV) curve of MPC-900 shows an obvious cathodic peak located at 0.80 V in O_2-saturated solution (Fig. S17), suggesting the occurrence of the ORR on MPC-900 electrode. From the linear sweep voltammetry (LSV) curves in Fig. 5A, compared to VB-900, MPCs exhibit a drastic enhancement in the ORR activities with an increase in current density and a positive shift in half-wave potential ($E_{1/2}$). Among MPCs, MPC-900 is identified as the best catalyst toward the ORR, showing the most positive $E_{1/2}$ of 0.85 V. To further clarify the ORR kinetics of the most active MPC-900, the RDE measurements were carried out at various rotating speeds from 400 to 2400 rpm. Fig. 5B shows that the current density increases with the increase of rotation rate, probably arising from the improved mass transport and the shortened diffusion distance. The corresponding Koutecky–Levich (K–L) plots (insert of Fig. 5B) represents a good linearity, implying the first-order reaction kinetics toward the concentration of dissolved oxygen.[29] The average transferred electron number was calculated from the slope of K–L plots to be about 3.8 at the potential from 0.76 to 0.61 V, which indicates that the oxygen reduction is predominantly taking place via a nearly four-electron pathway with hydroxyl as the main product. Figure 5C shows a low Tafel slope of 53 mV dec^{-1} on MPC-900,

validating that the rate-limiting step is the transfer of first electron in the ORR process, a mechanism that is commonly invoked for a Pt/C catalyst.[30] The activity of MPC-900 is also compared with that of a commercial 20% Pt/C catalyst. It is observed that MPC-900 presents a comparable ORR activity with the Pt/C in terms of the close $E_{1/2}$ (0.85 vs. 0.85 V) and higher kinetic-limiting current density at 0.71 V (51 vs. 17 mA cm^{-2}). Besides the excellent ORR activity of MPC-900, it also exhibits a high stability (Fig. S18). To the best of our knowledge, the ORR activity of MPC-900 is among the highest activities of reported porous carbon-based catalysts (Table S3), making MPC-900 a promising alternative to the precious Pt/C as a cathodic electrocatalyst in alkaline fuel cells.

The development of electrolysis CO_2-to-fuel technology is hindered by the lack of suitable catalyst for the CO2RR because CO_2 is a fully oxidized and thermodynamically stable molecule.[31] We further exploited the possibility of applying MPCs for the CO2RR in aqueous $KHCO_3$ electrolyte. For the LSV curve in Ar-saturated solution, the current is ascribed to the reduction of proton to H_2. When Ar supply is replaced by CO_2, reaction current increases, implying the occurrence of the CO_2 reduction in addition to the proton reduction (Fig. S19). The gaseous products after electrolysis were analyzed by a gas chromatograph (GC) equipped with a thermal conductive detector (TCD) and flame ionization detector (FID), and the liquid-phase products were investigated by ^1H NMR spectroscopy. The detected gas-phase products include main CO and H_2, as well as extremely few CH_4, which account for more than 98 % of the total Faradaic efficiency (FE, Fig. S20). No liquid-phase products were detected. As shown by the FE and partial current density for CO on MPCs in Fig. 6A, B, CO_2 reduction on MPC-1000 starts at −0.3 V with FE of 10%, meaning a low overpotential of −0.190 mV. MPC-1000 is identified as the most efficient catalyst for the CO2RR with the maximum FE of 62 % and current density of 3.1 mA cm^{-2} at the potential of −0.7 V (overpotential of −0.59 V) for CO. It is also found that the FE of CO is highly dependent on the applied potential, which shows a volcano-type characteristic. Specifically, the FE increases as a more negative potential is applied (from 10% at −0.3 V to 62% at −0.7 V). When potential sweeps more negatively than −0.7 V, the FE of CO decreases probably because the mass transfer of CO_2 to electrode surface becomes the rate-determining step instead of thermodynamics, resulting in a decline in the CO2RR rate and increase in proton reduction rate (Fig. S20). To obtain insight into the electrokinetic pathway for CO2RR on MPC-1000, the Tafel plot is presented (Fig. 6C), which is linear over the potential range from −0.3 to −0.5 V with a slope of 129 mV dec^{-1}. This Tafel slope demonstrates that the rate-determining step is probably associated with the initial one electron transfer to CO_2 with the formation of a surface adsorbed $*CO_2^{\bullet-}$ intermediate on N,P,Co-induced active sites, as evidenced by the similar Tafel slope on carbon-based catalysts and metal catalysts.[32-34] With the participation of two protons and another one electron, the $*CO_2^{\bullet-}$ is further reduced to CO*, and the subsequent desorption of CO* from MPC-1000

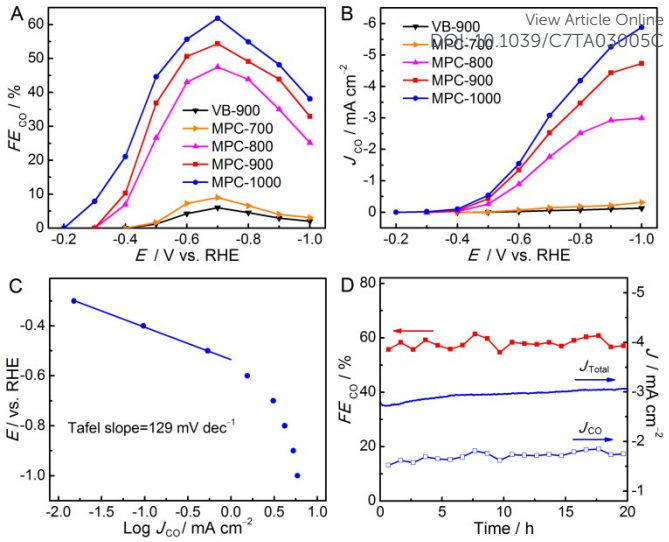

Fig. 6 (A) Faradaic efficiency and (B) partial current density for CO at different various potentials in CO_2-saturated 0.1 M $KHCO_3$. (C) Tafel plot and (D) electrochemical stability at −0.6 V for CO on MPC-1000 in CO_2-saturated 0.1 M $KHCO_3$.

results in the production of CO. Moreover, the Tafel slope of MPC-1000 is smaller than some of the reported heteroatoms-doped carbon nanotube, graphene and metal-organic frameworks.[23,34-36] The smaller Tafel slope implies that the overpotential rises slowly with increase of current density, thus suggesting a fast rate of MPC-1000 in the CO2RR process. The stability of MPC-1000 for CO2RR is depicted in Fig. 6D by the 20 h of continuous electrolysis. The result reveals that MPC-1000 does not show the attenuation in FE and current density for CO production, signifying the extraordinary durability. In view of the low Tafel slope, small overpotential and high FE compared with other carbon-based catalysts (Table S4), our MPC-1000 would be a feasible electrocatalysts in CO_2 electrolysis application, especially for the production of syngas with variable compositions.

Previous studies have proposed possible electrocatalytic active centers for the ORR and CO2RR on heteroatoms-doped carbons, which are suggested to be derived from the alteration of electronic structure and spin density of carbon atoms induced by heteroatoms-created dopants.[37-44] For N,P,Co-doped MPCs frameworks, the catalytic groups might be the C–N, C–P, Co–N_X and Co_2P species. Based on the activities results that MPCs prepared at different temperature exhibit distinct differences in their catalytic activities for the ORR and CO2RR, it is concluded that the heating temperature has great effect on the catalytic origin of MPC. This may be resulted from the variation of texture properties and N,P,Co compositions/configurations caused by the varied pyrolysis temperature. In this case, the 900 °C is found to be the optimal temperature to produce the most active MPC-900 for the ORR. The enhancement in ORR activity from 700 to 900 °C may be resulted from the increase in graphitization degree (Fig. S14) and surface area (Table 1), which endows MPCs with high

electrical conductivity to transfer electron and provide an enhanced exposure of surface active group to improve the sites utilization efficiency in the electrocatalytic process, respectively. The overheating at 1000 °C leads to the decline in the ORR activity. This may be due to the severe decrease in contents of doped atoms (Table S2), leading to the decrease in the total number of active groups, albeit the surface areas are also enhanced. Moreover, MPC-900 has a highest content of pyridinic N, which can also bind with Co to form Co−N_X complex. It is generally known that the pyridinic N is one of the most active dopants for the ORR as doping N in pyridinic configuration can create the adjacent Lewis base carbon sites that adsorbs oxygen molecules as the initial step in the ORR process.[45,46] The Co−N_X complex was also demonstrated to be extremely efficient in the ORR to promote the ORR along a $4e^-$ pathway.[47,48] We propose that these two kinds of dopants play dominate catalytic roles in the ORR, despite the functions of other C−N and C−P group cannot be totally ignored. As for CO2RR, MPC-1000 shows the best activity among the series, different with the ORR. The active sites in the CO2RR on N,Co-containing carbons has been suggested to be the C−N and Co−N_X.[32,40,49] The reported results demonstrated that the most efficient N chemical state for the CO2RR is the graphitic N, which can stabilize the $CO2^{\bullet-}$ radical anion, thereby lowering the initial activation barrier and improving the intrinsic activity.[30] We noticed that the MPC-1000 has the highest percentage of graphitic N (about 50%), proved by XPS analyses, which may serve as the primary site coupled with other N,P,Co-created species for the CO2RR. The MPC-1000 also has the highest surface area of 1036 m^2 g^{-1} and pore volume of 2.55 cm^3 g^{-1}, which may also be a significant thrust to boost the selectivity of MPC-1000 for the CO2RR as the increased electrode mesostructure (surface area, porosity) has been suggested to be a principal factor to suppress the hydrogen evolution and increase the selectivity for the CO2RR.[50] On the other hand, we observed that MPC-900 exhibit significantly enhanced activity for the ORR and CO2RR than non-porous VB-900. This reflects the crucial role of the mesopore in the electrocatalytic process, which may efficiently increase the number of active dopants on the mesopore edges and facilitate the mass transportation, contributing largely to electrochemical performance. Therefore, the enhanced electrocatalytic performance of MPCs can be ascribed to the effective integration of the N,P,Co-induced active dopants and mesoporous architecture with high surface area, and an ideal balance between surface area, porosity, conductivity, contents and chemical configurations of N,P,Co might be significant to achieve the excellent performance for ORR and CO2RR.

Experimental

Preparation of MPCs. In a typical procedure, 150 mg Vitamin B_{12} and 20 g NaCl were added into 150 mL DI-water under stirring to obtain uniform solution. The solution was frozen at −20 °C for more than 50 h, and water was eliminated by a freeze-drying process to form VB-NaCl mixture. Then, VB-NaCl was transferred into a crucible (30 ml) with a cover, which was placed into a quartz tube (length: 100 cm, diameter: 7 cm) and heated by a tubular furnace (GSL-1600X) at 900 °C for 3 h with a heating rate of 3 °C min^{-1} under Ar flow (180 sccm). After being cooled to room temperature, the product was washed thoroughly with hot water for four times to eliminate NaCl, which was dried in a vacuum oven at 70 °C overnight to yield powdered MPCs.

Electrochemical ORR Activity Measurements. The ORR was performed in a three-electrode configuration in 0.1 M KOH electrolyte (pH=13). A Pt wire and a saturated Ag/AgCl were used as the counter and reference electrodes, respectively. The potential was calibrated with respect to reversible hydrogen electrode (RHE) according to E(vs. RHE) = E (vs. Ag/AgCl) + 0.197 V + 0.0591×pH. To prepare the working electrode, the 4 mg catalyst was dispersed in 1 mL mixture solution (0.75 mL water, 0.21 mL ethanol and 40 µL 5wt% Nafion) by sonication for 5 h. Then, 5 µL well-dispersed ink was dropped onto a glassy carbon (3 mm in diameter) surface, and dried at room temperature. Prior to tests, 0.1 M KOH was bubbled with high-purity Ar/O_2 to saturate electrolyte. The CV was cycled with a scan rate of 50 mV s^{-1} and LSV was recorded with a sweep rate of 5 mV s^{-1} at different speed rates. For comparison, the 20 wt% Pt/C for ORR was also conducted by using the same procedure.

The kinetic parameters of ORR can be calculated based on the Koutecky−Levich (K−L) equations as follows:[51]

$$1 / J = 1 / J_L + 1 / J_K$$

$$J_L = 0.62 \cdot F \cdot D_0^{2/3} \cdot \upsilon^{-1/6} \cdot C_0 \cdot n \cdot \omega^{1/2} = K \cdot n \cdot \omega^{1/2}$$

$$K = 0.62 \cdot F \cdot D_0^{2/3} \cdot \upsilon^{-1/6} \cdot C_0$$

Where J is the measured current density using RDE, J_L is the diffusion-limiting current density, J_K is the kinetic-limiting current density, F is the Faraday constant (96,485 C mol^{-1}), D_0 is the diffusion coefficient of O_2 in electrolyte (1.9×10^{-5} cm^2 s^{-1}), υ is the kinetic viscosity in electrolyte (0.01 cm^2 s^{-1}), C_0 is bulk concentration of O_2 in electrolyte (1.2×10^{-6} mol cm^{-3}), n is the number of transferred electrons, and ω is the disk electrode rotation rate. K reflects the physical-chemical properties of the electrolyte. According to the K−L plots (J^{-1} is the y-axis, and $\omega^{-1/2}$ is the x-axis), the J_K can be obtained via the interception of the K−L plots, and n can be estimated from the slope of the K−L plots.

Electrochemical CO2RR Activity Measurements. The CO2RR was carried out in a home made two-compartment three-electrode electrochemical cell in CO_2-saturated 0.1 M $KHCO_3$ electrolyte (pH=6.8). A Pt and Ag/AgCl were used as the counter electrode and reference electrodes, respectively. The working electrode was prepared by drop casting 40µL of catalysts ink onto carbon paper (1 cm^2). The ink was prepared by dispersing 3 mg catalyst in solution of 300 µL DI-water, 270 µL isopropanol, and 30 µL 5% Nafion solution via sonication for 5 h. The working and reference electrodes were placed in the cathode chamber, while counter electrode was placed in the anode chamber, which was separated by a piece of Nafion 115 ionic exchange membrane. The high purity CO_2 was introduced in the cathode chamber for 1 h before electrolysis, and Ar was introduced in the anode chamber. The flow rate was measured to be 34 ml min^{-1} by a Gilian Gilibrator 2 Calibration System.

The gas phase products were analyzed by using an online gas chromatograph (GC, Fuel Cell GC-2014ATF, Shimadzu) equipped with a thermal conductivity detector (TCD) and a methanizer assisted flame ionization detector (FID). The liquid-products were identified by a nuclear magnetic resonance (NMR) spectrometer. 2,2,3,3-d(4)-3-(trimethylsilyl)propionic acid sodium salt (TSP) was used as the internal standard, and the 0.6 mM TSP standard solution was prepared in D_2O. The sample for ^1H NMR was prepared by depositing 500 μl of the $KHCO_3$ solution after electrolysis in NMR tube followed by adding 100 μl of STP standard solution.

The Faradaic efficiency (FE) of gas phase products at each applied potential was calculated based on the equation as follows:[32,52]

$$\mathrm{FE} = (z \cdot P \cdot F \cdot V \cdot v_i)/(R \cdot T \cdot j)$$

Where z is the number of electrons transferred per mole of gas product (z is 2 for CO and H_2, z is 8 for CH_4), P is pressure (1.01×10^5 Pa), F is Faraday constant (96500 C mol^{-1}), V is the gas flow rate (5.67×10^{-7} m^3 s^{-1}), v_i is the volume concentration of gas product determined by GC, T is the temperature (298.15 K), and R is the gas constant (8.314 J mol^{-1} K^{-1}). j is the current at each applied potential. The partial current density for CO is determined by calculating the total current density multiplied by FE of CO.

Conclusions

In summary, we have developed a new self-constructing protocol to fabricate 3D N,P,Co-doped MPCs frameworks via a self-growth-templating approach. It is worthy highlighted that the self-formation and removal of the mesoporous templates, and in situ incorporation of the N,P,Co functionalities are achieved simultaneously in an enclosed space-assisted pyrolysis process. Benefiting from the N,P,Co-induced dopants as the highly active centers, mesoporous architecture to increase sites density and to promote mass delivery, and high surface area to enhance sites exposure, MPCs can serve as the bifunctional electrocatalysts for the oxygen and CO_2 reduction. The optimized MPCs exhibit the outstandingly intrinsic activities for the ORR with a positive $E_{1/2}$ of 0.85 V, a high J_K of 51 mA cm^{-2} at −0.71 V and a low Tafel slope of 53 mV dec^{-1}, as well as for the CO2RR in terms of a low overpotential of −0.19 V, a maximum FE of 62% for CO and a small Tafel slope of 129 mV dec^{-1}, along with high stability for both reactions. The palmary performance renders MPCs frameworks promising electrocatalysts systems in fuel cells and CO_2 conversion technologies. More importantly, the self-growth-templating concept proposed here represents a major breakthrough in the development of heteroatoms-functionalized MPCs to gain the enhanced electrochemical performance, which is also believed to potentially bring an innovation on the methodology for synthesizing other mesoporous materials beyond carbon for the broad applications.

Acknowledgements

This work was supported by the National Key Basic Research and Development (973) Program of China (2013CB632300) and Natural Science Foundation of Ningbo (No. 2015A610241 and 2016A610109).

Notes and references

1 J. Liu, N. P. Wickramaratne, S. Z. Qiao and M. Jaroniec, *Nat. Mater.*, 2015, **14**, 763-774.
2 S. Chen and S.-Z. Qiao, *ACS Nano*, 2013, **7**, 10190-10196.
3 D. D. Zhu, J. L. Liu and S. Z. Qiao, *Adv. Mater.*, 2016, **28**, 3423-3452.
4 M. K. Debe, *Nature*, 2012, **486**, 43-51.
5 M. B. Stevens, L. J. Enman, A. S. Batchellor, M. R. Cosby, A. E. Vise, C. D. M. Trang and S. W. Boettcher, *Chem. Mater.*, 2017, **29**, 120-140.
6 M. Asadi, B. Kumar, A. Behranginia, B. A. Rosen, A. Baskin, N. Repnin, D. Pisasale, P. Phillips, W. Zhu, R. Haasch, R. F. Klie, P. Král, J. Abiade and A. Salehi-Khojin, *Nat. Commun.*, 2014, **5**, 4470.
7 T. Palaniselvam, M. O. Valappil, R. Illathvalappil and S. Kurungot, *Energy Environ. Sci.*, 2014, **7**, 1059-1067.
8 W. Ding, L. Li, K. Xiong, Y. Wang, W. Li, Y. Nie, S. Chen, X. Qi and Z. Wei, *J. Am. Chem. Soc.*, 2015, **137**, 5414-5420.
9 S. Lee, M. Choun, Y. Ye, J. Lee, Y. Mun, E. Kang, J. Hwang, Y.-H. Lee, C.-H. Shin, S.-H. Moon, S.-K. Kim, E. Lee and J. Lee, *Angew. Chem. Int. Ed.*, 2015, **54**, 9230-9234.
10 Y.-Z. Chen, C. Wang, Z.-Y. Wu, Y. Xiong, Q. Xu, S.-H. Yu and H.-L. Jiang, *Adv. Mater.*, 2015, **27**, 5010-5016.
11 Y. Meng, D. Voiry, A. Goswami, X. Zou, X. Huang, M. Chhowalla, Z. Liu and T. Asefa, *J. Am. Chem. Soc.*, 2014, **136**, 13554-13557.
12 J. Wei, Y. Liang, X. Zhang, G. P. Simon, D. Zhao, J. Zhang, S. Jiang and H. Wang, *Nanoscale*, 2015, **7**, 6247-6254.
13 B. Bayatsarmadi, Y. Zheng, M. Jaroniec and S. Z. Qiao, *Chem Asian J*, 2015, **10**, 1546-1553.
14 Z. Li, G. Li, L. Jiang, J. Li, G. Sun, C. Xia and F. Li, *Angew. Chem. Int. Ed.*, 2015, **54**, 1494-1498.
15 T. C. Nagaiah, A. Bordoloi, M. D. Sánchez , M. Muhler and W. Schuhmann, *ChemSusChem*, 2012, **5**, 637-641.
16 J. Tang, J. Liu, C. Li, Y. Li, M. O. Tade, S. Dai and Y. Yamauchi, *Angew. Chem. Int. Ed.*, 2014, **54**, 588-593.
17 J. Qin, C. He, N. Zhao, Z. Wang, C. Shi, E.-Z. Liu and J. Li, *ACS Nano*, 2014, **8**, 1728-1738.
18 U. B. Nasini, V. Gopal Bairi, S. Kumar Ramasahayam, S. E. Bourdo, T. Viswanathan and A. U. Shaikh, *ChemElectroChem*, 2014, **1**, 573-579.
19 J. P. Paraknowitsch, Y. Zhang, B. Wienert and A. Thomas, *Chem. Commun.*, 2013, *49*, 1208-1210.
20 D. Yan, S. Dou, L. Tao, Z. Liu, Z. Liu, J. Huo and S. Wang, *J. Mater. Chem. A*, 2016, **4**, 13726-13730.
21 B. Kumar, M. Asadi, D. Pisasale, S. Sinha-Ray, B. A. Rosen, R. Haasch, J. Abiade, A. L. Yarin and A. Salehi-Khojin, *Nat. Commun.*, 2013, **4**, 2819.
22 U. Sim, T.-Y. Yang, J. Moon, J. An, J. Hwang, J.-H. Seo, J. Lee, K. Y. Kim, J. Lee, S. Han, B. H. Hong and K. T. Nam, *Energy Environ. Sci.*, 2013, **6**, 3658-3664.
23 P. P. Sharma, J. Wu, R. M. Yadav, M. Liu, C. J. Wright, C. S. Tiwary, B. I. Yakobson, J. Lou, P. M. Ajayan and X.-D. Zhou, *Angew. Chem.*, 2015, **127**, 13905-13909.
24 F. Pan, S. Guo and J. Zhang, *Electrochim. Acta*, 2015, **180**, 29-36.
25 Y. Zhu, B. Zhang, X. Liu, D.-W. Wang and D. S. Su, *Angew. Chem. Int. Ed.*, 2014, **53**, 10673-10677.
26 A. Morozan, P. Jegou, B. Jousselme and S. Palacin, *Phys. Chem. Chem. Phys.*, 2011, **13**, 21600-21607.

View Article Online
DOI: 10.1039/C7TA03005C

27 S. Yang, L. Zhi, K. Tang, X. Feng, J. Maier and K. Müllen, *Adv. Funct. Mater.*, 2012, **22**, 3634-3640.
28 J. Zhang, Z. Zhao, Z. Xia and L. Dai, *Nat. Nano.*, 2015, **10**, 444-452.
29 K. J. J. Mayrhofer, D. Strmcnik, B. B. Blizanac, V. Stamenkovic, M. Arenz and N. M. Markovic, *Electrochim. Acta*, 2008, **53**, 3181-3188.
30 A. Kongkanand, S. Kuwabata, G. Girishkumar and P. Kamat, *Langmuir*, 2006, **22**, 2392-2396.
31 Q. Lu and F. Jiao, *Nano Energy*, 2016, **29**, 439-456.
32 J. Xu, Y. Kan, R. Huang, B. Zhang, B. Wang, K.-H. Wu, Y. Lin, X. Sun, Q. Li, G. Centi and D. Su, *ChemSusChem*, 2016, **9**, 1085-1089.
33 C. W. Li and M. W. Kanan, *J. Am. Chem. Soc.*, 2012, **134**, 7231-7234.
34 N. Kornienko, Y. Zhao, C. S. Kley, C. Zhu, D. Kim, S. Lin, C. J. Chang, O. M. Yaghi and P. Yang, *J. Am. Chem. Soc.*, 2015, **137**, 14129-14135.
35 J. Wu, R. M. Yadav, M. Liu, P. P. Sharma, C. S. Tiwary, L. Ma, X. Zou, X.-D. Zhou, B. I. Yakobson, J. Lou and P. M. Ajayan, *ACS Nano*, 2015, **9**, 5364-5371.
36 J. Wu, S. Ma, J. Sun, J. I. Gold, C. Tiwary, B. Kim, L. Zhu, N. Chopra, I. N. Odeh, R. Vajtai, A. Z. Yu, R. Luo, J. Lou, G. Ding, P. J. A. Kenis and P. M. Ajayan, *Nat. Commun.*, 2016, **7**, 13869.
37 K. Gong, F. Du, Z. Xia, M. Durstock and L. Dai, *Science*, 2009, **323**, 760-764.
38 M. Kim, D.-H. Nam, H.-Y. Park, C. Kwon, K. Eom, S. Yoo, J. Jang, H.-J. Kim, E. Cho and H. Kwon, *J. Mater. Chem. A*, 2015, **3**, 14284-14290.
39 G.-L. Tian, M.-Q. Zhao, D. Yu, X.-Y. Kong, J.-Q. Huang, Q. Zhang and F. Wei, *Small*, 2014, **10**, 2251-2259.
40 A. S. Varela, N. Ranjbar Sahraie, J. Steinberg, W. Ju, H.-S. Oh and P. Strasser, *Angew. Chem.*, 2015, **127**, 10908-10912.
41 H. Wang, Y. Chen, X. Hou, C. Ma and T. Tan, *Green Chem.*, 2016, **18**, 3250-3256.
42 Z. Liu, Z. Zhao, Y. Wang, S. Dou, D. Yan, D. Liu, Z. Xia and S. Wang, *Adv. Mater.*, 2017, **29**, 1606207.
43 L. Tao, Q. Wang, S. Dou, Z. Ma, J. Huo, S. Wang and L. Dai, *Chem. Commun.*, 2016, **52**, 2764-2767.
44 F. Pan, Q. Zhao, J. Wang and J. Zhang, *ChemElectroChem*, 2015, **2**, 2032-2040.
45 D. Guo, R. Shibuya, C. Akiba, S. Saji, T. Kondo and J. Nakamura, *Science*, 2016, **351**, 361-365.
46 H. Metiu, S. Chrétien, Z. Hu, B. Li and X. Sun, *J. Phys. Chem. C*, 2012, **116**, 10439-10450.
47 S. Kattel, P. Atanassov and B. Kiefer, *Phys. Chem. Chem. Phys.*, 2013, **15**, 148-153.
48 L. Shang, H. Yu, X. Huang, T. Bian, R. Shi, Y. Zhao, G. I. N. Waterhouse, L.-Z. Wu, C.-H. Tung and T. Zhang, *Adv. Mater.*, 2016, **28**, 1668-1674.
49 J. Shen, R. Kortlever, R. Kas, Y. Y. Birdja, O. Diaz-Morales, Y. Kwon, I. Ledezma-Yanez, K. J. P. Schouten, G. Mul and M. T. M. Koper, *Nat. Commun.*, 2015, **6**, 8177.
50 Y. Yoon, A. S. Hall and Y. Surendranath, *Angew. Chem. Int. Ed.*, 2016, **55**, 15282-15286.
51 R. Cao, R. Thapa, H. Kim, X. Xu, M. Gyu Kim, Q. Li, N. Park, M. Liu and J. Cho, *Nat. Commun.*, 2013, **4**, 2076.
52 M. S. Jee, H. S. Jeon, C. Kim, H. Lee, J. H. Koh, J. Cho, B. K. Min and Y. J. Hwang, *Appl. Catal. B: Environ.*, 2016, **180**, 372-378.